BBA - Molecular Basis of Disease 1870 (2024) 167330

Contents lists available at ScienceDirect

BBA - Molecular Basis of Disease

journal homepage: www.elsevier.com/locate/bbadis

A splice-altering homozygous variant in *COX18* causes severe sensory-motor neuropathy with oculofacial apraxia

Fabiola Mavillard [a,b,1], Alejandra Guerra-Castellano [c,1], David Guerrero-Gómez [d], Eloy Rivas [e], Gloria Cantero [a,b], Emilia Servian-Morilla [a,b], Chiara Folland [f], Gianina Ravenscroft [f], Miguel A. Martín [g,h], Antonio Miranda-Vizuete [d], Macarena Cabrera-Serrano [a,b], Irene Diaz-Moreno [c,*], Carmen Paradas [a,b,**]

[a] Neuromuscular Unit, Neurology Department, Instituto de Biomedicina de Sevilla (IBIS)/Hospital Virgen del Rocío/CSIC/Universidad de Sevilla, Spain
[b] Centro Investigación Biomédica en Red Enfermedades Neurodegenerativas (CIBERNED), Instituto de Salud Carlos III, Sevilla, Spain
[c] Instituto de Investigaciones Químicas, Universidad de Sevilla-CSIC, Sevilla, Spain
[d] Redox Homeostasis Group, Instituto de Biomedicina de Sevilla (IBIS)/Hospital Virgen del Rocío/CSIC/Universidad de Sevilla, Spain
[e] Department of Neuropathology, Hospital Universitario Virgen del Rocío, Sevilla, Spain
[f] Harry Perkins Institute of Medical Research, Centre for Medical Research, University of Western Australia, Nedlands, WA 6009, Australia
[g] Mitochondrial & Neuromuscular Disorders Group, Genetics Department, Hospital 12 de Octubre Research Institute (imas12), Madrid, Spain
[h] Biomedical Network Research Centre on Rare Diseases (CIBERER), Instituto de Salud Carlos III, Madrid, Spain

ARTICLE INFO

Keywords:
Encephaloneuropathy
Complex IV
COX18
Missplicing
Mitochondria
Supercomplex

ABSTRACT

Cytochrome-*c* oxidase (COX) is part of the mitochondrial complex IV (CIV). COX deficiency is usually associated with tRNA variants, and less frequently with variants in COX assembly factors. Mutations in COX subunits encoded by mitochondrial DNA and nuclear DNA are rare, likely because most of them are associated to very severe phenotypes with early lethality. COX18, an assembly factor of CIV, has long been analyzed as a potential cause of mitochondrial disease. To date, only one patient has been identified carrying a homozygous missense variant in *COX18,* associated with neonatal encephalo-cardiomyopathy and axonal sensory neuropathy. Here, we describe a 40-year-old patient, asymptomatic until 7 months of age, who presented with progressive muscle weakness resembling spinal muscle atrophy type-2, associated with oculofacial apraxia and dysarthric speech. Electrophysiology analysis highlighted a severe sensory-motor neuropathy. Muscle biopsy showed striking and diffuse decreases of COX staining and a substantial reduction of CIV activity. Muscle biopsy showed no ragged-red fibers, although ultrastructural mitochondrial alterations were evident. A novel homozygous variant (c.598G>A), located in the last nucleotide of exon 3, was detected in *COX18* by whole-exome sequencing, which affected the splicing donor site, as demonstrated by cDNA-seq. The patient fibroblasts express a truncated form of COX18 (COX18Δ112-240) capable of assembling CIV and CIV-involving supercomplexes. However, CIV activity was decreased. COX18 full-length (COX18-fl) overexpression partially rescued CIV activity in the patient fibroblasts. The rescue of the null CIV activity in COX18-KO-HEK293 cells by overexpressing of COX18Δ112-240 was significantly lower than in cells with COX18-fl. In addition, *cox-18* downregulation in *C. elegans* resulted in slow growth and, diminished reduced motility phenotypes and as well as severe fragmentation of the mitochondrial network. Our case expands the phenotypes associated with *COX18* variants and supports the pathogenic role of *COX18* as the cause of a severe encephaloneuropathy syndrome.

* Corresponding author.
** Correspondence to: C. Paradas, Neuromuscular Unit, Neurology Department, Instituto de Biomedicina de Sevilla (IBIS)/Hospital Virgen del Rocío/CSIC/Universidad de Sevilla, Spain.
E-mail addresses: idiazmoreno@us.es (I. Diaz-Moreno), cparadas@us.es (C. Paradas).
[1] These authors have been contributed equally to this work.

https://doi.org/10.1016/j.bbadis.2024.167330
Received 16 April 2024; Received in revised form 23 June 2024; Accepted 25 June 2024
Available online 1 July 2024

1. Introduction

Mitochondria are fundamental organelles for the functioning of eukaryotic cells, because they are the main energy producer and participate in many cellular processes [1]. Inside mitochondria, metabolic reactions of high interest occur (Krebs cycle, β-lipid oxidation, *etc.*), among which the electronic transport chain (ETC) stands out. The correct functioning, assembly, and regulation of the ETC components is essential for cell survival and energy metabolism [2–6]. Alterations in some of its components are related to a wide variety of diseases, such as mitochondrial myopathy and, Leber's hereditary optic neuropathy, as well as the aging phenomenon itself [7–10].

Cytochrome *c* oxidase (COX) is the mitochondrial respiratory chain complex IV (CIV) which catalyzes the oxidation of cytochrome *c* (Cytc) coupled with the reduction of molecular oxygen to water. Mammalian COX consists of 14 subunits: three mitochondrial DNA (mtDNA) encoded subunits that comprise the catalytic core of COX (COX1, COX2, and COX3), and 11 nuclear DNA (nDNA) encoded subunits that play essential roles in COX stability and activity regulation (COX4, COX5A, COX5B, COX6A, COX6B, COX6C, COX7A, COX7B, COX7C, COX8A and NDUFA4/COXFA4) [11–20]. COX assembly proceeds as a modular process, compassing several steps that require a high number of assembly factors [13,21,22]. COX1 and COX2 contain the CIV redox-active metal centers, which are involved in electrons transfer, while COX3 is the cyclooxygenase. The maturation process of COX2 is of special interest due to its links with human pathologies. Mature COX2 comprises two transmembrane domains and an elongated unstructured hydrophilic C-terminal towards the intermembrane space (IMS), which harbors the binuclear copper center (Cu_A). The N-terminal transmembrane domain region of COX2 needs to be inserted into the inner mitochondrial membrane (IMM) and subsequently stabilized through interactions with COX20 [23]. COX18 is also a transmembrane protein in the Oxa1/YidC/Alb3 family of membrane protein insertases; it facilitates, the export of the COX2 C-terminal across the IMM [12]. Finally, the incorporation of copper atoms into the Cu_A center is mediated by the SCO1, SCO2, and COA6 metallochaperones [24] (Fig. 1).

COX deficiency, particularly in muscle, is usually found associated with tRNA mutations, and less frequently to mutations in the COX assembly factors. In contrast, mutations in mtDNA- or nDNA-encoded COX subunits are unusual [13], and many of these mutations are associated with very severe phenotypes with early lethality. The hypothesis that COX assembly factors could be associated with isolated COX deficiency in muscle led to a study of the *COX18* in 29 patients with different clinical phenotypes. This study found no pathogenic variants encoded by *COX18* [25]. Recently, however, a unique case of severe neonatal encephalo-cardiomyopathy and axonal sensory neuropathy was reported to be associated with a homozygous pathogenic variant in *COX18* [26].

Here, we report a novel biallelic pathogenic variant in *COX18*, which affects its splicing, that is associated with a pure neurological phenotype of infantile onset, with clinical manifestations due to central and peripheral nervous system alterations. Our case expands the phenotypes associated with *COX18* variants and supports the pathogenic role of COX18 as the cause of a severe encephaloneuropathy syndrome.

2. Materials and methods

2.1. Ethical compliance and patient information

The study was approved by the local Ethics Committee at Hospital Universitario Virgen del Rocío. Informed consent was obtained from the patients and healthy controls. We describe a patient from a consanguineous family. Clinical examinations, muscle biopsies and genetic analysis were performed.

2.2. Muscle biopsy

Muscle samples were obtained by open biopsy from the deltoid muscle at age 36, and processed following standard procedures. Briefly, fresh muscle samples were frozen in liquid nitrogen. Frozen sections (6 μm thick) were prepared for the histochemical staining hematoxilin-eosin, Gomori trichrome and combined COX/Succinate dehydrogenase (SDH). Mitochondrial respiratory chain complex activity was measured in muscle. Southern blot analysis of mtDNA extracted from muscle was performed to study the presence of deletions.

2.3. Genetic study

Patient's genomic DNA was extracted from blood using standard procedures. After checking the quality, the human gene exons were captured and massively sequenced using the MedExome assay and NextSeq equipment (Illumina, San Diego, CA) with an average depth of coverage >30×. Segregation analysis was performed in the patient's relatives. DNA was extracted from blood using standard procedures and the *COX18* variation was detected by Sanger sequencing, using the primers 5′-CCACCCTTTCAAAGCCACTG-3′ (annealing at exon 3) and 5′-CAGGAAAGATCTGCACTGGA-3′ (annealing at intron 3–4).

Patient's muscle whole mitochondrial DNA (mtDNA) genome massive sequencing was performed using long-range PCR amplification of mtDNA following the protocols established for the PGM-Ion Torrent sequencer (Life Technologies, Carlsbad, CA). Variant calling, annotation and prioritization were carried out using a pipeline that integrates variant calling format (VCF) files with the Mitomap database (www.mitomap.org) and MitImpact predictors (https://mitimpact.css-mendel.it).

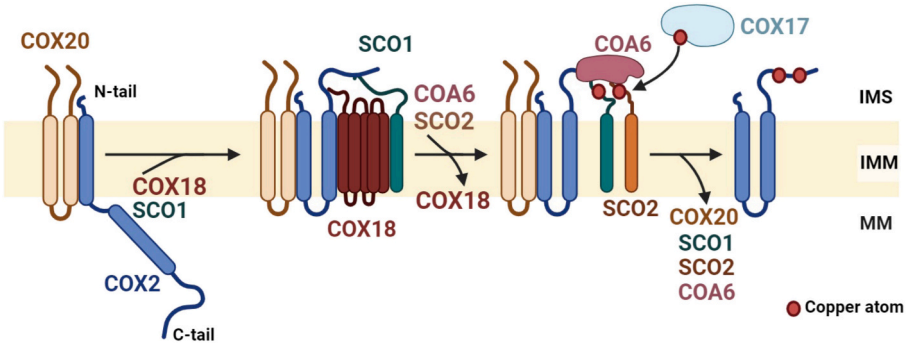

Fig. 1. COX assembly model. COX20 contributes to stabilizing COX2 as its N-terminal transmembrane domain undergoes insertion. Subsequently, COX18 engages with C-tail of COX2 to aid its translocation across the inner mitochondrial membrane. COX18 mediates the interaction of SCO1 with the ensemble and concomitantly is dissociated allowing the binding of the SCO1-SCO2-COA6 module. COX17 delivers the copper atoms to SCO proteins. SCO1 is the metallochaperone that inserts copper into COX2, while SCO2 and COA6 facilitate the copper transfer, thereby finalizing the process of COX2 biogenesis. IMS: intermembrane mitochondrial space; IMM: inner mitochondrial membrane; MM: mitochondrial matrix.

2.4. Fibroblasts and cell line cultures

Human skin biopsies were cultured following the MRC CNMD Biobank London protocol (TC2 fibroblast isolation from skin biopsy, V6 24/05/2013). Briefly, human skin samples were minced and consecutively incubated with trypsin and collagenase solution. After the digestion, the cellular disaggregate was grown in DMEM containing 10 % fetal bovine serum and 1 % penicillin–streptomycin–fungizone at 37 °C with 5 % CO_2. The first fibroblasts were visible after approximately 2 days. Once the cells approached to confluency, they were trypsinized and reseeded, to increase cell purity. The COX18-KO-HEK293 stable cell line was generated by TALEN technology [12] and kindly provided by Dr. Barrientos (University of Miami Miller School of Medicine). The cell lines were grown in DMEM containing 10 % fetal bovine serum, 50 μg/mL uridine, 110 μg/mL sodium pyruvate, and 1 % penicillin–streptomycin. Mitochondrial respiratory chain complexes activity was measured in fibroblasts.

2.5. Electron microscopy

Fibroblasts from the patient and two healthy controls were trypsinized and washed with PBS by centrifugation. Cell pellets were fixed for 1 h in 2 % glutaraldehyde in cacodylate buffer (0.1 M sodium cacodylate, 2 mM $MgCl_2$) at 4 °C. After three washing steps (5 min each one), samples were post fixed for 1 h at 4 °C in 1 % OsO_4 in the same buffer. After three washing steps (20 min each one), the samples were immersed in 2 % uranyl acetate, dehydrated through a gradient acetone series (50 %, 70 %, 90 % and 100 %), and embedded in Spurr resin. Blocks were obtained by polymerization at 70 °C for 8 h. Thin sections were cut with a diamond knife in an ultramicrotome (Leica UC7) and examined with a transmission electron microscope (Zeiss Libra 120) operating at 80 kV. The electron microscopy images were taken at different magnifications with an EMCCD camera (TRS 2k × 2k).

2.6. Mitochondrial network analysis

Live cells were stained with 100 nM MitoTracker® Red CMXRos (Cell Signaling, Massachusetts, USA. cat. No. M7512) for 30 min, fixed, and mounted on slides using Fluoromount-G™ mounting medium, with DAPI (Thermofisher Scientific, Waltham, MA, cat. No. 00-4959-52). Images were captured with confocal A1R (NIKON, Tokio, Japan). For 2D mitochondrial network morphological analysis, semi-automated analysis was performed with the Mitochondrial Network Analysis method (MiNA) macro toolset as previously described [27] on the FIJI distribution of the ImageJ platform (National Institutes of Health). Briefly, from a confocal image, a binary image, a binary image was created with foreground pixels set to the maximum value (255) and background pixels to the minimum value (0). Skeletonization of binary images represents the features of the original image as a wireframe of lines one pixel wide. The binary image enables us to delineate the area covered by the mitochondrial network (footprint), whereas skeletonized imaging allows us to analyze individual mitochondria, mitochondria that are part of a network, and the size of this network. With this tool, the quality of the images is improved by pre-processing steps before converting them into binary images, producing a morphological skeleton to calculate the morphology of the mitochondrial network.

2.7. RT-PCR and qRT-PCR analyses

Total RNA was extracted from fibroblast culture from the patient, two healthy controls, and a disease control, using a tissue RNA purification kit (Norgen, cat. No. 17200). Immediately following extraction, a PrimeScript™ RT Master Mix kit (Takara, Kusatsu Japan, cat. No. RR036A) was used to obtain cDNA. For RT-PCR analysis, *COX18* cDNA was amplified using the primers 5′-GCCTACCAGCACTACATCCT-3′ (annealing at exon 1) and 5′-CGAAATCCAGGAGAACGCAG-3′ (annealing at exon 5). PCR products were analyzed by gel electrophoresis and sequenced by Sanger method. qRT-PCR was performed by TaqMan® method in the 7500 Fast Real-Time PCR System. Relative mRNA levels were compared using the $2^{-\Delta\Delta CT}$ method, using GAPDH as a control. To detect *COX18* mRNA, two different probes that annealed at the 2–3 and the 5–6 exon boundary (Hs00403166 and Hs01087679, respectively) were used. To analyze mitochondrial stress, probes against PPARGC1A cDNA (PGC-1α) (Hs00173304) were used.

2.8. Western blot analysis

Fibroblasts were homogenized in RIPA buffer (20 mM Tris–HCl pH 7.4, 150 mM NaCl, 1 mM EDTA, 1 % IGEPAL, 0.1 % SDS) containing protease inhibitor mixture. Equivalent amounts of protein lysates were resolved on SDS-PAGE gels and transferred to PDVF membranes (Millipore). To study COX1, COX2 and COX4 proteins, rabbit polyclonal anti-COX-1 (Proteintech, cat. No. 13393-1-AP), mouse monoclonal antibody (COX 229) (Invitrogen, cat. No. 35-8200) and rabbit polyclonal anti COX-4 (Genetex, cat. No. GTX101499) were used. Immunoreactivity was detected with secondary antibodies conjugated to horseradish peroxidase (Jackson Immuno Research) and developed with SuperSignal West Femto (Thermo Scientific) using an ImageQuant LAS 4000 MiniGold System (GE Healthcare). Polyclonal rabbit anti-GAPDH (Sigma-Aldrich, cat. No. G9545) was developed as a loading control.

2.9. Lentivirus generation and infection

COX18 full-length (*COX18*-fl) cDNA was kindly provided by Dr. Barrientos (University of Miami Miller School of Medicine) and cloned into pLVET-IRES-GFP (Addgene, Plasmid #107139), to produce pLVET-COX18-fl-IRES-GFP. To generate pLVET-COX18Δ112-240-IRES-GFP, the double PCR technique was used. Lentiviral particles were generated based on the calcium phosphate method as previously described [28]. Briefly, HEK293T cells were transfected using the transfer plasmids pLVET-IRES-GFP, pLVET-COX18-fl-IRES-GFP or pLVET-COX18Δ112-240-IRES-GFP, together with psPAX2 packaging (Addgene, plasmid #12260) and pMD2.G envelope plasmid DNA (Addgene, plasmid #12259) at a ratio of 4:3:1, respectively. At 72-h post-transfection, the medium was collected, filtered, and concentrated by centrifugation for 90 min at 105,000 ×*g* using a SW32-Ti Beckman rotor. Supernatant was completely removed, and pellet diluted in 100 μl PBS overnight at 4 °C, titered by FACS, and stored at −80 °C until use. Fibroblasts from the controls or the HEK293T cell line were infected with pLVET-IRES-GFP; COX18-KO-HEK293 cells were infected with pLVET-COX18-fl-IRES-GFP or pLVET-COX18Δ112-240-IRES-GFP; and the patient's fibroblasts were infected with pLVET-COX18-fl-IRES-GFP. After 7 days, GFP-positive cells were purified by FACS. At confluence, cells were harvested by trypsinization.

2.10. Isolation of mitochondria from cell lines

Mitochondria from fibroblasts, HEK293 cell lines and infected cells (for rescue assays) were obtained by differential centrifugation as reported previously [29]. The medium was removed from the cells and washed once with PBS, then cells were detached using a cell scraper, and the cell suspension was transferred to a 50 mL polypropylene tube. Cells were centrifuged at 600 *g* at 4 °C for 10 min, the supernatant was discarded, and cells were resuspended in 3 mL of ice-cold isolation buffer (IB_c: 10 mM Tris-MOPS, 1 mM EGTA/Tris and 200 mM sucrose, pH 7.4). Cells were placed in a glass pot to homogenize and were stroked 30–40 times. The homogenate was transferred to a 50 mL tube, and centrifuged at 600 *g* for 10 min at 4 °C, then the supernatant was collected and centrifuged at 7000 *g* for 10 min at 4 °C. The supernatant was discarded, the pellet was washed with 200 mL of ice-cold IB_c buffer, resuspended in 200 mL of ice-cold IB_c, and the suspension was transferred to a 1.5 mL microfuge tube. The homogenate was centrifuged at 7000 *g* for 10 min at

4 °C, the supernatant was discarded, and the pellet containing mitochondria was resuspended in 0.05 mL of IBc buffer. Isolated mitochondria were preserved at −80 °C in IB_c until further use.

2.11. Blue-native gel electrophoresis

Mitochondrial pellets (400 μg) were resuspended and incubated in 40 μL of solubilization buffer (30 mM HEPES buffer [pH 7.4], with 150 mM KOH-acetate, 10 % glycerol and 1 mM PMSF) plus digitonin at a digitonin:protein ratio of 4:1 (w:w) on ice for 30 min. Samples were then centrifuged for 30 s to eliminate mitochondria membrane debris and determined the supernatant concentration by Bradford assay. Samples were loaded onto a pre-cast NativePAGE™ Novex® 3–12 % polyacrylamide Bis-Tris gel (1.0 mm, 15-well; Thermo Fisher Scientific, cat. No. BN2012BX10), following the manufacturer's instructions for performing a blue-native gel electrophoresis (BN-PAGE) using the XCell™ SureLock™ Mini-Cell (Thermo Fisher Scientific, cat. No. EI0001). Briefly, gel was run for 90 min at 150 V and were stained for protein detection with 0.25 % Coomassie Brilliant Blue R-250 in a solution of 45 % methanol and 10 % acetic acid. The band size estimation may have an expected size estimation error of ~15 %.

2.12. Tryptic digestion analysis

For protein identification, the band of the BN-PAGE gel were subject to tryptic digestion analysis. For this purpose, acrylamide gel bands were treated with ammonium bicarbonate and acetonitrile, followed by reduction of disulfide bonds using dithiothreitol (DTT) and carbamidomethylation of cysteine residues with iodoacetamide. Samples were incubated overnight at 37 °C with bovine trypsin at ratio 1:10 (enzyme: substrate). After acetonitrile extraction and acidification, samples were desalted and concentrated with C18-filled tips. Measurements were performed in a MALDI-TOF Ultraflextreme system (Bruker) configured on positive reflectron mode. For each spectrum, results of 3000 laser shots were averaged. MALDI mass fingerprint spectra were analyzed searching against specific COX18Δ112-240 sequence and results were filtered using a 0.01 % protein FDR threshold [30]. The spectra were recorded at the Biomolecular Mass Spectrometry Service of the Pablo de Olavide University.

2.13. Cytochrome c oxidase activity

COX activity was measured to evaluate the functionality of complex IV in the presence of COX18-fl or COX18Δ112-240. To achieve this, the oxidation of exogenous reduced Cytc by endogenous COX in isolated mitochondria samples was monitored. Cytc exhibits a sharp absorption band at 550 nm when reduced, which weakens and broadens upon oxidation. The BioChain's Mitochondria Activity Assay Kit (Newark, CA, USA, cat. No. KC310100) is a spectrophotometric assay that measures the decrease in absorbance at 550 nm of reduced Cytc by COX. The detergent n-dodecyl β-D-maltoside (βDDM) was used to permeate the outer mitochondrial membrane and allow exogenous human wild-type Cytc (final concentration of 6.9 μM) to penetrate. The COX reaction follows first-order kinetics relative to Cytc concentration, showing exponential decay. The assay measures the first-order rate constant within the initial 55 s of the reaction. COX activity is expressed in units of μmol of reduced Cytc/mL of mitochondrial sample per min (unit/mL). The COX activity values have been calculated from slopes of absorbance at 550 nm from at least three independent measurements as previously reported [31].

2.14. Caenorhabditis elegans

2.14.1. Strains

The standard methods used for culturing and maintenance of *C. elegans* were as previously described [32]. The strains used in this study were N2 wild type (DR subclone of CB original); NL2099, *rrf-3 (pk1426) II*; VZ977, *rrf-3(pk1426) II*; *jIs01[Pmyo-3::gfp::myo-3; rol-6 (su1006)]*; UTA59, *rrf-3(pk1426) II*; *zcIs13[Phsp-6::gfp] V*; VZ986, *ccIs4251[Pmyo-3::gfp-LacZ(NLS); Pmyo-3::mitogfp; dpy-20(+)] I*; and *rrf-3(pk1426) II*.

2.14.2. RNA interference

cox-18 RNAi downregulation was performed by feeding worms with *E. coli* HT115 bacteria expressing cox-18 dsRNA (clone IV-1.Q.2.E02 Julie Arhinger RNAi library, confirmed by sequencing). HT115 bacteria expressing the plasmid pL4440 were used as the RNAi control. A single colony of the corresponding bacteria was inoculated into LB with ampicillin (100 μg/mL) and incubated at 180 rpm and 37 °C overnight. Then, NGM plates supplemented with carbenicillin (25 μg/mL) and IPTG (1 mM) were seeded with 100 μL of the overnight culture and incubated at 37 °C for 48 h. Unless otherwise noted, all experiments were performed on synchronized worms generated by allowing 10 to 15 gravid hermaphrodites (previously grown for two generations on the respective RNAi bacteria) to lay eggs for 2–3 h on RNAi seeded plates at 20 °C.

2.14.3. Image acquisition and processing

Image acquisition was carried out in animals paralyzed with 10 mM levamisole on a microscope slide in an Olympus BX61 fluorescence microscope equipped with a DP72 digital camera coupled to CellSens Software. When needed, ImageJ, Adobe Photoshop and Adobe Illustrator Software were used for quantification and processing of the micrographs.

2.14.4. Morphological and stress phenotype

The analysis of morphological and stress phenotypes was analyzed as described: The *rrf-3(pk1426)* worm strain was used to quantify the length, area, number of oocytes in the proximal arm of the posterior gonad and gonad migration phenotypes; *rrf-3(pk1426);jIs01* to visualize muscle cell myofilament integrity; *rrf-3(pk1426);zcIs13* to quantify mitochondrial unfolded protein response (UPR^{mt}) induction; and *ccIs4251;rrf-3(pk1426)* to determine the extent of mitochondrial fragmentation. All experiments were performed in animals grown for 72 h at 20 °C.

2.14.5. Motility phenotypes

The motility of rrf-3 with downregulated cox-18 expression was determined in liquid and solid medium (*via* thrashing and bending, respectively) for worms grown for 72 h at 20 °C. For motility in liquid medium, worms were picked individually and transferred to a 5 μL drop of M9 buffer on top of microscope slide and allowed to acclimate for 1 min and the head thrashes were counted during the following minute on a stereomicroscope. For motility in solid medium animals were picked individually and transferred to a 35 mm NGM seeded Petri's plate and allowed to acclimate for 1 min and the body bends were counted during the following minute on a stereomicroscope.

2.15. In silico calculations

Methods and associated references for conducting "3D Structure prediction and molecular dynamics simulation", "Predicting protein–membrane interactions", and performing "Molecular docking" can be found in the *Supplementary Information*.

2.16. Statistics

Graphs and statistical analyses were made using GraphPad Prism software. Data are mainly represented as violin plots, showing the distribution of the data, median values, and the interquartile ranges, except for Mitochondrial Network Analysis (MiNA).

To confirm normal distribution, the Shapiro-Wilk test was applied.

As the sample size was too small to confirm normal distribution, the non-parametric Kruskal-Wallis tests were used to examine statistical significance. Mann-Whitney tests were used for pairwise comparisons. Statistical significance levels were set to $p < 0.05$ with Bonferroni correction for multiple pairwise comparisons.

3. Results

3.1. The patient presents spinal muscular atrophy (SMA)-like motor phenotype with oculofacial apraxia

We describe a 40-year-old man from a consanguineous family without any developmental concerns until the age of 7 months (Fig. 2A), at which point, after a vaccination followed by fever and exanthema, he presented progressive weakness. He was able to stand up with knee-ankle-foot orthesis (KAFO) but did not achieve independent gait, and he had rapid progression of lower and upper limbs weakness, muscle atrophy, and need for a wheelchair in early infancy (Fig. 2A). At the age of sixteen, he developed respiratory involvement with the need for non-invasive mechanical ventilation starting at the age of 25. He frequently presents episodes of acute muscle weakness involving limb and axial muscles, spontaneously solved after 24 h, sometimes following mild infections. Examination at age of 24 showed normal cognition (he is qualified chess player). Oculomotor and facial apraxia were evident (Videos S1 and S2), with slow and dysarthric speech. He presented general hypotonia, severe muscle weakness with atrophy in distal and proximal muscles, ankle contractions, and global areflexia. Vibratory, proprioceptive and pain sensation were severely affected in lower legs and hands.

Nerve conduction studies at the ages of 4 and 28 years showed the lack of compound motor action potential in lower limbs, with markedly reduced amplitude in upper limbs. Sensory action potentials were absent in cubital and sural nerves. Needle study of the tibialis anterior muscle showed motor unit potentials with severe neurogenic features with scattered fibrillations and positive waves. Cranial tomography and electroencephalography at 4 years of age, and cranial MRI at 24 years of age, showed normal findings. The serum CK level was normal between 4 and 24 years of age. Forced vital capacity was 55 % and 28 % at the ages of 16 and 24, respectively. All cardiologic exams were normal during follow-ups.

3.2. Muscle biopsy shows a neurogenic pattern without ragged-red fibers

Muscle biopsy showed a severe adipose replacement, fibrosis, and atrophy (Fig. 2B). We observed entire fascicles full of atrophic fibers, alternating with fascicles formed of normal or slightly hypertrophic myofibers, with occasional angulated atrophic fibers and some nuclear clumps. There were no ragged-red fibers, which would indicate excessive mitochondrial proliferation, and no necrotic fibers. NADH and SDH staining showed irregular intermyofibrillar pattern with oxidative defects, unique and well-defined (pseudocores) or multiple, small, and irregular (moth-eaten fibers), which indicate alterations in mitochondrial distribution into the myofiber. ATPases showed fibers type grouping and predominance of type I fibers, consistent with denervation and reinnervation processes. COX/SDH combo staining showed a severe diffuse reduction of COX staining in all the fibers and a severe decrease in COX activity, which was 46 % below the lower normal limit. The enzyme activity value of complex IV found in the patient's muscle was 18.38 nmol/min/mg protein, while reference values are in the range of 34–180 nmol/min/mg protein. The activity of the other complexes of the respiratory chain was within the normal range.

3.3. Identification of a homozygous variant in COX18

We detected a novel homozygous missense variant in *COX18* by whole-exome sequencing (WES). The variant, *COX18* c.598G>A (NM_173827.4), p.Gly200Ser, localizes in the last nucleotide of the third exon, and was predicted to affect the donor splice site. We confirmed the presence of the variant by Sanger sequencing (Fig. 2C), and its co-segregation with the disease by segregation analyses of the DNA from available relatives (Fig. 2D). The variant does not have an entry in gnomAD genomes; however, the *COX18* locus is covered in 88.05 % of samples above 20× coverage. Nonetheless, the variant is present with 0.049 % allele frequency in a Spanish Collaborative Variability Server (CSVS), which contains >2000 genomes and exomes of unrelated Spanish individuals [33]. Pathogenicity predictor tools based on amino acid sequence analysis, as Polyphen2 [34], Provean [35], and SIFT [36] have classified the *COX18* c.598G>A variant as benign. However, those tools that consider additional factors, such as the splicing process, (Mutation Taster [37], dbscSNV [38], and FATHMM-MKL [39]), classified the variant as likely pathogenic. The splicing site predictor varSEAK (varseak.bio) predicted exon skipping (100 %, class 5). Following the American College of Medical Genetics (ACMG) guidelines, the variant is classified as a variant of uncertain significance (VUS). No candidate variants were prioritized in muscle mtDNA. Exome analysis did not identify any additional homozygous variants that could explain the clinical phenotype in the patient, the isolated and severe reduction of COX activity, and that segregate with the disease (Table S1).

3.4. Mitochondria ultrastructural alteration

Electron microscopy of the patient's fibroblasts showed more electrodense mitochondria with increased fragmentation compared to control, but normal cristae morphology. The cytoskeleton appeared partially disrupted, and an increased autophagosome formation and mitophagy was observed as compared to those of the controls (Fig. 3A). We analyzed confocal images of fibroblasts using MitoTracker staining through MiNA methods [27]. The quantification of the binary images demonstrated an increased mitochondrial footprint in the patient samples as compared to the control samples (Fig. 3B). Skeletonization of binary images showed the same number of networks but an increased number of mitochondria (individuals) and branching size in the patient samples, consequently leading to an increased network (Fig. 3C). The marker of mitochondrial stress *PGC-1α* mRNA showed a higher expression in patient's fibroblast compared to healthy controls and to fibroblasts from a patient with a mitochondrial myopathy due to a homozygous variant in thymidine kinase 2 gene (*TK2*) (Fig. 3D).

3.5. mRNA analysis suggests the expression of a truncated form of the COX18 protein

To investigate whether the *COX18* c.598G>A variant affects splicing, we examined the PCR results of cDNA from skin fibroblast total RNA. We obtained a band with the expected size in three different PCR experiments using control fibroblasts. In contrast, we did not observe this band from the patient sample; instead, we observed three PCR products of smaller sizes (Fig. 4A). Sequencing analysis of the cDNA in these bands revealed that each was the result of a failure in the splicing process during mRNA maturation. Specifically, the largest PCR product lacked the exon 3; the medium one lacked the exons 3 and 4; and the smallest one lacked exons 2, 3, and 4 (Fig. 4B).

To confirm this result, we used qRT-PCR with two different probes: one probe that binds to the exon 2–3 boundary, and a second probe that binds to the junction of exons 5–6, present in all the PCR products obtained. Indeed, the exon 5–6 boundary probe amplified all transcripts, while the exon 2–3 boundary probe amplified the transcript only from the control samples but not from the patient sample (Fig. 4C).

Analysis of the PCR product sequences indicated that transcripts from the medium and largest bands, but not from the smaller band, were the result of a frameshift, which is degraded through the process of nonsense-mediated decay [40]. *In silico* translation of the smaller band corresponded to the sequence NM_173827.4, which lacked the amino

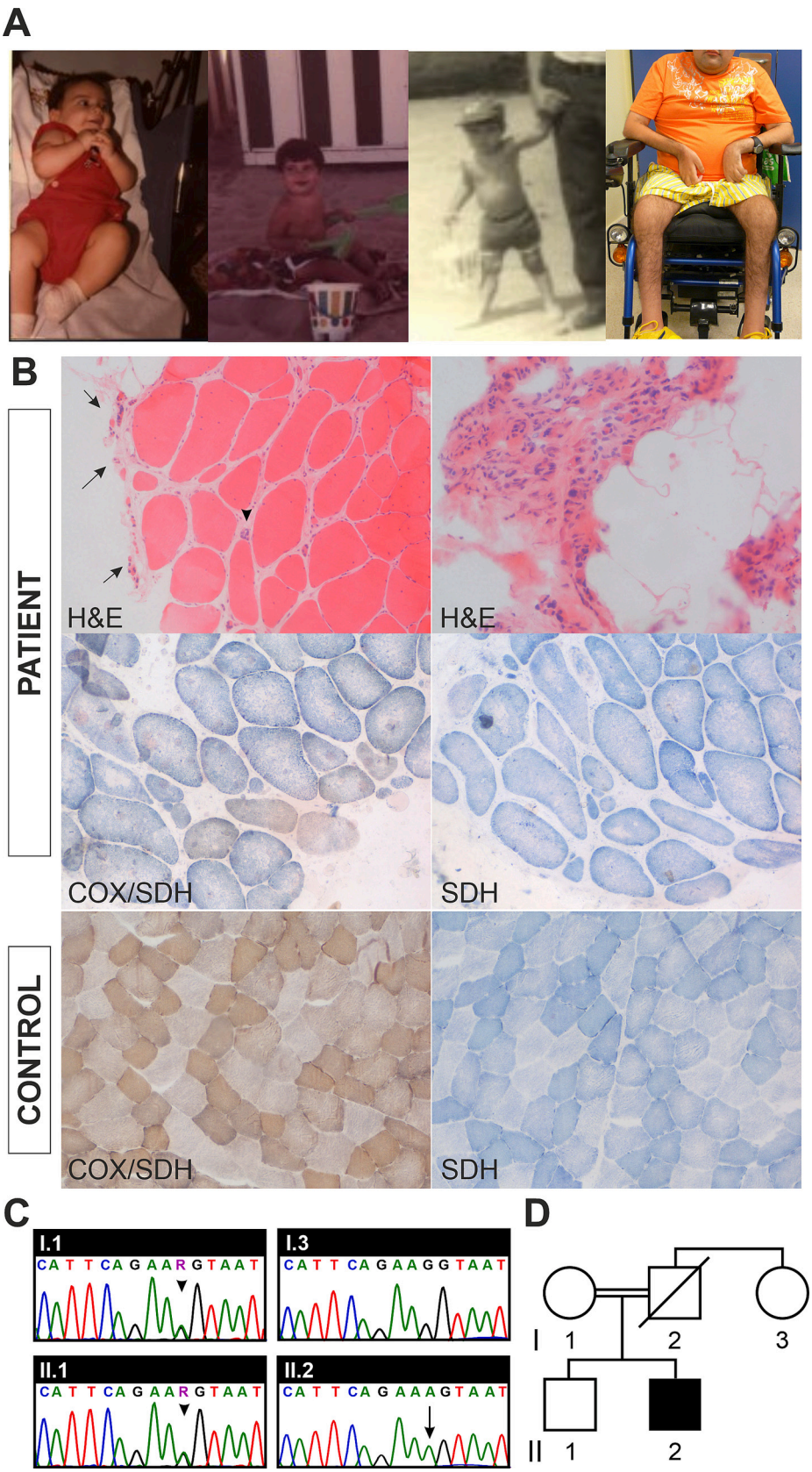

(caption on next page)

Fig. 2. Clinical features, muscle biopsy and genetic data. A. Patient's pictures show a normal motor development during the first seven months of life (pictures 1 and 2), need for KAFO at the age of 1 year (picture 3) and further need for wheelchair (picture 4), due to severe weakness and muscle atrophy in four limbs. B. Muscle biopsy showed with H&E increased fibrosis and fatty replacement with some fascicles full of atrophic fibers alternated with better preserved fascicles showing nuclear clumps (arrowhead) and some groups of atrophic fibers in the periphery (arrow). Combined SDH/COX staining showed a severe diffuse reduction of COX staining in most fibers, which is obvious compared to control. Notice the complete absence of mitochondrial proliferation signs (no red or blue ragged fibers). C. Electropherograms of the genomic DNA Sanger sequencing shows the homozygous *COX18* c.598G>A variant in the patient (arrow), the heterozygous variant in the mother and brother (arrowhead), and the absence of this variant in the paternal aunt. D. Family pedigree shows the relatives in whom the *COX18* variant was sequenced.

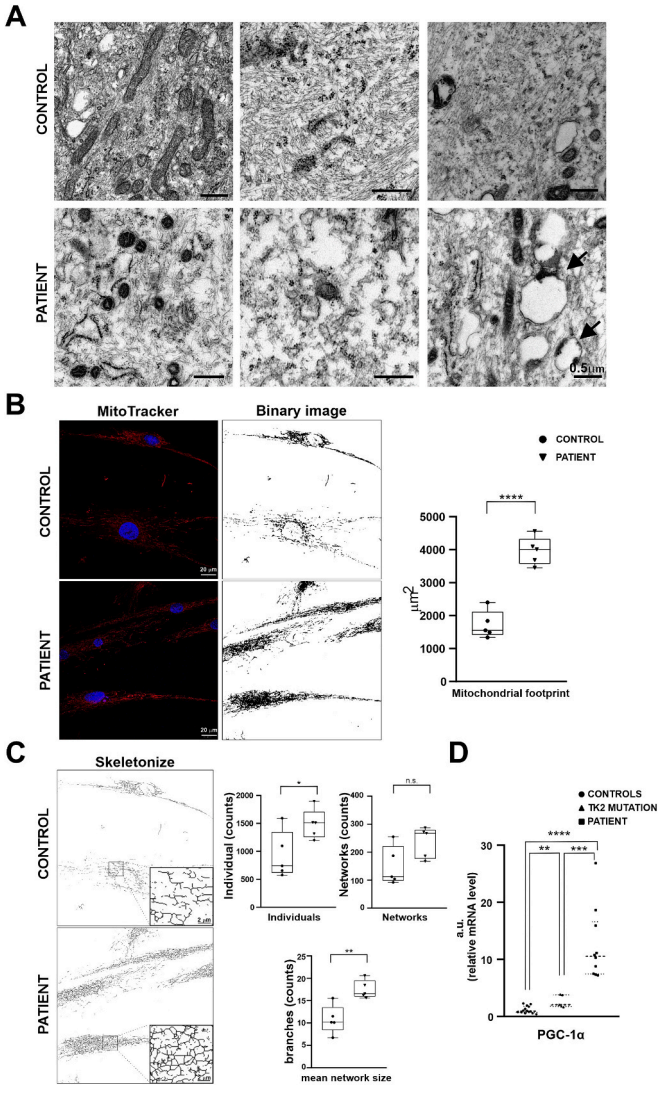

Fig. 3. Mitochondrial alterations. A. Electron microscopy of patient fibroblasts show more fragmented and electro-dense mitochondria with normal cristae, cytoskeleton is partially disrupted, and autophagosome formation and mitophagy are increased (arrows), compared to control. B. Mitochondrial Network Analysis (MiNA) of MitoTracker confocal images in fibroblast from patient and controls shows increased mitochondrial footprint in the patient. C. Skeletonisation of binary images shows the same amount of networks but an increased number of mitochondria (individuals) and branching size in the patient, resulting in an increased network size in patients compared to controls. D. *PGC-1α* mRNA expression, a marker of mitochondrial stress, is increased in fibroblasts from this patient compared to controls and a patient with a different mitochondrial disorder (*TK2* mutation).

acids from Val112 to Glu240 (Fig. S1A).

The 3D molecular modeling of the 204-residue sequence corresponding to the truncated COX18 protein (COX18Δ112-240) showed structural similarity to COX18-fl, including a disordered N-end towards the IMS that elongates α-helix onto IMM (Fig. S1B). However, two transmembrane α-helices along with the helix-turn-helix motif oriented towards MM are missing in COX18Δ112-240 (Fig. S1B). In addition, the remaining three transmembrane α-helices of COX18Δ112-240 are slightly tilted with respect to the ones in COX18-fl (Fig. S1B). The hydrophobic thickness, which defines how the protein sits within the hydrocarbon core of the lipid bilayer that surrounds it in a membrane, remained unaltered between both proteins.

3.6. Lesser amounts of functional complex IV are assembled in the presence of the truncated COX18 protein

First, we demonstrated that the mutated protein COX18Δ112-240 was expressed in the patient fibroblasts (Fig. S2). Notably, the patient fibroblasts showed a largely reduced level of COX2 protein, but similar level of COX1 and COX4 subunits, as compared to the control fibroblasts (Fig. 5A). This decrease is likely attributed to an increase in proteolysis of unassembled COX2, consistent with previous reports [12], rather than a substantial decrease in the level of mRNA encoding COX2.

To analyze the assembly of complex IV together with supercomplexes formation we examined the respiratory chain components in isolated mitochondria by BN-PAGE analysis. No substantial differences were found in the BN-PAGE band patterns, along with band intensities, between control- and patient-derived mitochondria, supporting that either the CIV assembly by COX18Δ112-240 or supercomplex formation remained unaltered (Fig. 5B). The presence of COX18Δ112-240 in the CIV-band of patient fibroblasts by tryptic digestion providing further evidence that truncated COX18 participates in the assembly of CIV (Fig. S2). However, differences in the mode of molecular recognition between truncated COX18Δ112–240 and COX2 regarding COX18-fl cannot be ruled out.

COX activity of COX18Δ112–240-including CIV in patient-derived mitochondria was significantly diminished, with an enzymatic activity 7.5 times lower that measured in mitochondria of healthy control individuals (Fig. 5C). Thus, patient with COX18Δ112-240 should suffer serious dysfunction in their mitochondrial energetic metabolism, as above mentioned. To explore molecular features that explain such differences in COX activity, we performed docking calculations to compare COX2:COX18-fl and COX2:COX18Δ112-240 ensembles, using HADDOCK software [41]. The resulting docking solutions (clusters) were grouped into a main clump, indicating a single binding site for COX2 on the surface of both COX18 proteins (Fig. 6). Moreover, an analysis of clusters organized by root mean square deviation (RMSD) showed that the binding site of COX2 in COX18-fl was well-defined and restricted to the surrounds of the helix-loop-helix motif, which is missing in COX18Δ112-240 (Fig. S3). Consequently, the larger number of clusters identified for the COX2:COX18Δ112-240 ensemble suggests that COX2 explores a broader region of the truncated COX18 surface, leading to a less defined binding site. The thermodynamic analysis of the molecular docking results showed that both complexes are driven by electrostatic and non-polar interactions (Tables S2 and S3) [42]. However, the major differences between the two types of ensembles are due to non-polar contacts, most favorable for COX18-fl-involving complexes with a large, buried surface area (Tables S2 and S3) [42].

We further explored the possible crosstalk between COX18-fl and COX18Δ112-240 by transfecting the patient's fibroblasts with a lentivirus overexpressing COX18-fl and recording COX activity. The activity measured in isolated mitochondria from the patient fibroblasts infected with a lentivirus expressing COX18-fl was three times higher than that

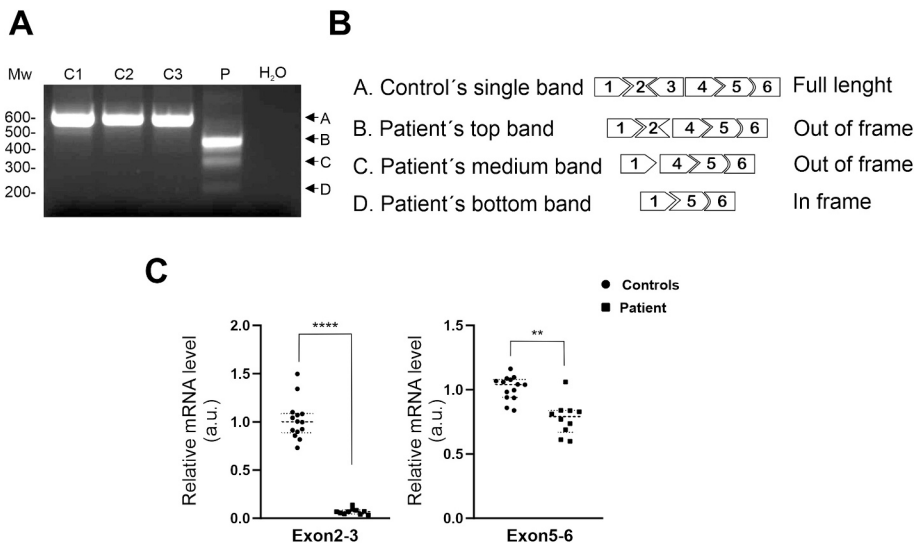

Fig. 4. *COX18* c.598G>A affects splicing. A. Total RNA extracted from fibroblast, retrotranscribed to cDNA and amplified by PCR, show three products of smaller sizes in the patient (P) compared to controls (C1–C3). Mw: molecular weight marker (Kb). Bands marker with arrows are schematically represented in panel B. B. The sequencing of each band showed in the largest PCR product a skipping of exon 3 (B), in the medium-size done an absence of exons 3 and 4 (C), and in the smallest one an absence of exons 2, 3 and 4 (D), supporting an alteration of the splicing. C. qRT-PCR confirmed the presence of undegraded truncated transcript in the patient using different probes. One probe aligned to the exon 2/3 junction, absent in the patient's transcript, and a second probe aligned to the exon 5/6 junction, present in both the patient and controls.

from mitochondria from the non-infected patient fibroblasts. However, COX activity did not recover to 100 % (Fig. 5C and D). The infection with the empty lentivirus expression vector ruled out secondary effects on COX activity due to cell infection, as can be observed in the activity recorded in mitochondria of healthy individual fibroblasts (Fig. 5C and D).

Using WT and COX18-KO-HEK293 cell lines we have dept into the possible interference between COX18-fl and COX18Δ112-240. As previously reported [12], neither CIV nor respiratory supercomplexes were assembled in COX18-KO-HEK293 cells. Upon infection of COX18-KO-HEK293 cells with a lentivirus expressing COX18Δ112-240, the levels of COX activity measured were substantially lower than those with COX18-fl (with about 1.5× less activity; Fig. 5E). However, COX activity was fully restored in COX18-KO-HEK293 cells infected with a lentivirus expressing COX18-fl (Fig. 5E), which supports the potential crosstalk between the wild-type and truncated COX18 proteins observed in the mitochondria from fibroblasts of the patient.

3.7. cox-18 depletion showed morphological anomalies, fragmentation in the mitochondrial network, and impaired mobility in Caenorhabditis elegans

Despite the low level of amino acid sequence identity between COX18 proteins from human and *C. elegans* (26.76 %), the 3D structural models are very similar to each other (Fig. S4). Based on this similarity, we used *cox-18* RNAi knock-down in *C. elegans* to explore phenotype features by depleting COX18-encoding gene. *cox-18* downregulation in a *C. elegans* wild-type strain produced no visible phenotypes. However, *cox-18* downregulation in a *rrf-3(pk1426)* mutant strain causes hypersensitivity to RNA interference [43], and worms display a slow growth phenotype [44]. Therefore, we decided to perform all subsequent RNAi experiments in a *rrf-3(pk1426)* mutant background.

rrf-3 animals with decreased *cox-18* expression had a sick, less turgid appearance and, consistent with the previous report [44], showed a significant reduction in body length and area as compared to control animals (Fig. 7A). At the morphological level, *cox-18* downregulated animals displayed obvious germline phenotypes consisting of aberrant gonad migration and decreased production of oocytes (Fig. 7B). However, we did not find any gross alteration of the myofibers as determined by the integrity of myofilaments along the longitudinal axis of the muscle cells (Fig. 7C).

We next aimed to evaluate whether mitochondria of *cox-18* downregulated animals were functionally compromised. We first evaluated the integrity of the mitochondrial network in the body muscle cells, which align in parallel to myofilaments along the longitudinal cell axis [45]. Using a transgene that expresses GFP in the mitochondrial matrix [19], we observed that decreased expression of *cox-18* caused a strong fragmentation of the muscle cell mitochondrial network, already obvious at day 3 after synchronized egg-lay (Fig. 6D). Consistently, *cox-18* downregulated animals displayed a robust induction of the *Phsp-6::gfp* reporter (Fig. 7E), which is a proxy for UPR^{mt} activation [46], demonstrating that *cox-18* downregulated animals were under severe mitochondrial stress. Consequently, *cox-18* downregulated animals exhibited diminished muscular function, measured as motility of worms in liquid and solid media (Fig. 7F and G).

4. Discussion

We report a patient with a pathogenic biallelic variant in *COX18* resulting in the production of truncated protein associated with an infantile form of sensory-motor neuropathy with oculofacial apraxia. Only one other case has been described, of a homozygous missense variant in *COX18*, the affected individual presented a neonatal encephalocardiomyopathy and axonal sensory neuropathy. Our study expands the phenotype and genotype linked to *COX18* deficiency and supports functional and molecular modeling studies for shedding light on the pathogenic effects caused by this variant, which affects splicing of *COX18* mRNA.

From a clinical perspective, the severe neurological phenotype, with involvement of both central and peripheral nervous system, are consistent with COX18 defects. COX18 is an assembly factor of the COX2. A review showed that all cases reported with causative variants in the assembly factors and subunits of this module presented a neonatal or infantile onset of severe neurological manifestations with encephalopathy, sensory axonal neuropathy, motor involvement with SMA features [47,48], even one case with mutation in *COX20* presented oculomotor apraxia [49] (Table S4). Notably, all of these clinical features are line with those in the patient reported here. In addition, the muscle biopsies

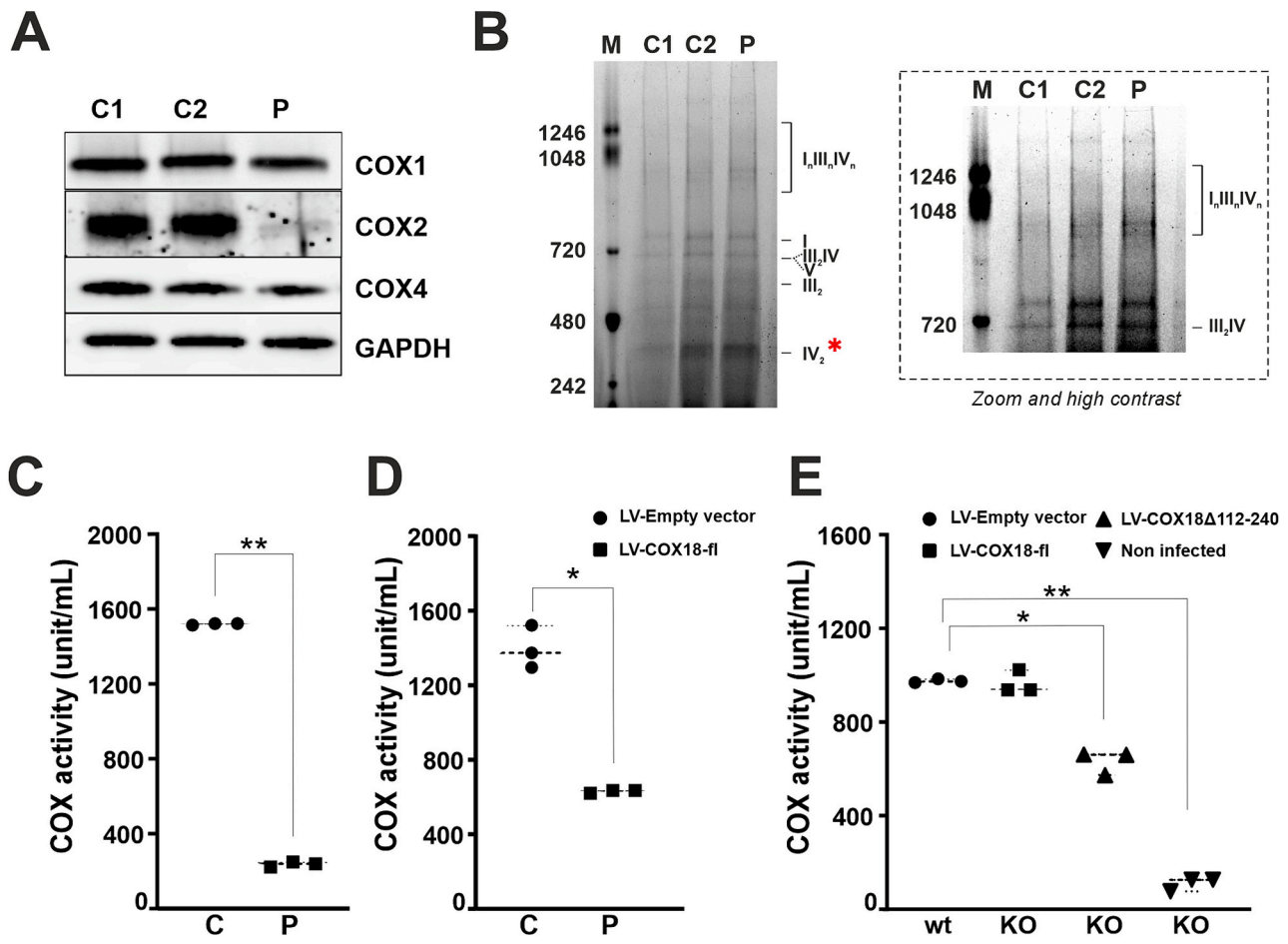

Fig. 5. Effect of COX18-fl and COX18Δ112-240 proteins on the functionality of complex IV, along with their impact on the assembly of respiratory supercomplexes. A. Western blot analysis of fibroblasts obtained from healthy individuals (C1 and C2) and the patient (P) reveals the abundance of COX1, COX2, and COX4 proteins. GAPDH is used as a loading control. B. BN-PAGE of mitochondria isolated from fibroblasts of healthy individuals (C1 and C2) and the patient (P). The hypothetical complex or supercomplex corresponding to each band is indicated on the right (I: complex I; III: complex III; IV: complex IV; V: complex V). The band submitted to tryptic digestion is highlighted by an asterisk. M: molecular weight marker (kDa). The inset shows a zoom and high contrast image of the supercomplexes region in the BN-PAGE gel. C. COX activity measured in mitochondria isolated from fibroblasts of healthy individuals (C) and the patient (P). D. COX activity was measured in isolated mitochondria from fibroblasts of healthy individual (C) infected with a lentivirus containing empty vector and from the patient's fibroblasts (P) infected with a lentivirus expressing COX18-fl. E. COX activity measured in isolated mitochondria from HEK293 cell lines infected with lentivirus expressing: empty vector for wild-type HEK293 (WT); COX18-fl, COX18Δ112-240 or without infection for COX18-KO-HEK293 (KO). All data included in panels C, D and E represent the mean ± SD of three independent experiments. Unit definition: One unit oxidizes one micromole of ferrocytochrome c/min at 25 °C, pH 7.0.

available from the reviewed cases show isolated CIV reduced activity, with uniform reduction or absence of COX histochemical staining, while the muscle morphological findings range from normal (in cases with isolated encephalopathy) to neurogenic pattern (in cases with motor neuropathy). Patients with mitochondrial disorders involving the peripheral nervous system use to display ragged red or ragged blue fibers in the muscle biopsy, as a sign of mitochondrial proliferation. Interestingly, none of the previously reported patients with mutations in genes involved in COX assembly show these types of fibers, neither the patient we report with the variants in *COX18*. Despite this, the electron microscopy and the structural analyses of the mitochondria in our patient's muscle and fibroblasts demonstrated profound mitochondrial morphological and network alterations. Thus, since we ruled out variants in other genes involved in CIV assembly, it is highly plausible that the clinical phenotype in the patient reported here was caused by the newly-reported *COX18* variant.

The information provided in the previously reported cases with mutations in proteins associated to CIV assembly, suggest that the amount of residual CIV activity is associated with the clinical severity, as reflected by fatal neonatal cases with early deaths and abortions due to SCO1 and SCO2 mutations, in which muscle biopsy showed COX-negative histochemical staining and minimal CIV residual activity [14,47,50–52]. In our case, the residual activity was higher than in previously reported cases, and the COX staining was reduced but not negative. This may could explain the infantile rather than neonatal onset, and the longer survival.

Fibroblasts from the patient reported here express a truncated form of COX18 that can assemble CIV and CIV-containing supercomplexes. This conclusion is based on the analysis of respiratory complexes and supercomplex assemblies by BN-PAGE, with similar pattern of bands for mitochondria isolated from healthy fibroblasts—expressing COX18-fl—and patient fibroblasts—expressing COX18Δ112-240. However, COX activity measured in mitochondria isolated from the patient showed a 90 % reduction, compared to control fibroblasts. Overexpression of COX18-fl partially rescued COX activity in the patient fibroblasts. This result suggests a competition for the binding site on COX2 between the endogenous COX18Δ112-240 and exogenous COX18-fl, since both COX18 proteins uses their surface area oriented towards the mitochondrial matrix to bind to COX2.

The rescue experiments performed in *wild type* and COX18-KO-HEK293 cell lines showed an approximately 40 % lower COX activity in COX18-KO-HEK293 cells expressing truncated COX18 than in cells

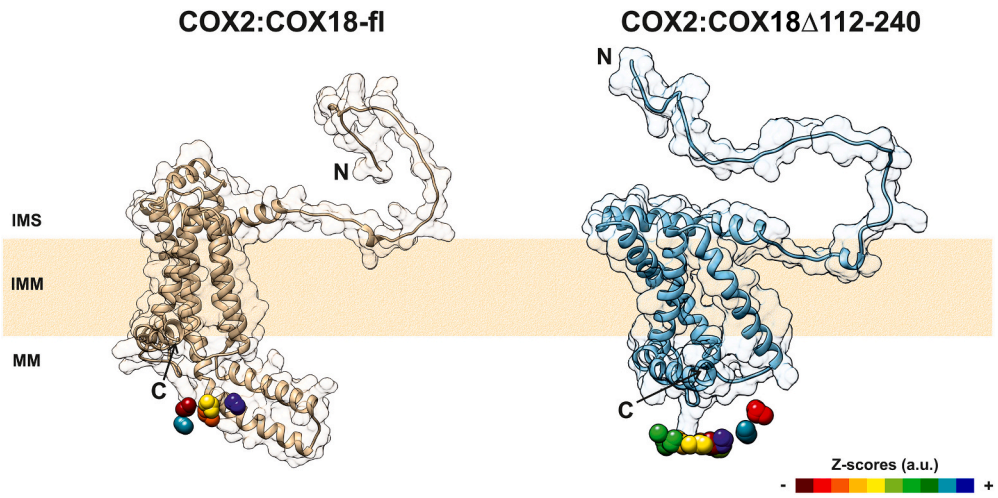

Fig. 6. The molecular interface of COX2:COX18 variants complex. Each complex shows the mass centers—plotted as a ball—of COX2, corresponding to the four lowest energy structures of each cluster. Balls are colored according to the Z-scores. The ribbon representation of COX18-fl (AlphaFold: AF-Q8N8Q8-F1) is colored in tan, and COX18Δ112-240 in blue. Z-score indicates how many standard deviations from the average this cluster is located in terms of score (the more negative, the better). IMS: intermembrane mitochondrial space; IMM: inner mitochondrial membrane; MM: mitochondrial matrix.

infected with lentivirus expressing COX18-fl. However, this decrease was not comparable to that in patient's fibroblasts (*ca.* 90 %). The discrepancy can be attributed to inherent differences between cell lines and primary cell cultures. The metabolic activity of immortalized cell lines is faster, which affects their ability to produce exogenous proteins. Additionally, they exhibit a less active antiviral response due to adaptations induced by immortalization, which allows for a higher expression of COX18Δ112-240.

In silico analyses of the COX2:COX18Δ112-240 interaction suggests the formation of a dynamic conformational ensemble rather than a single, well-defined complex. The dynamic ensemble broadens the range of conformational states, which may hinder the induced fit between the proteins. The buried surface area—which measures the size of the interface in a protein-protein complex in terms of solvent-accessible surface area—of truncated COX18 covered by COX2 was substantially smaller, in agreement with the suggested flexibility and plasticity of COX2:COX18Δ112-240 clusters. Furthermore, electrostatic contacts and the exclusion of water molecules were less favorable in complexes involving truncated COX18 protein (Tables S2 and S3). In other words, COX2:COX18Δ112-240 complex formation is energetically less favorable than the COX2:COX18-fl assemble.

Thus, we speculate that truncation of COX18 affects the binding and effective translocation of the COX2 C-tail, therefore, the integration of COX2 and its orientation at the IMM [45–47]. Since the C-tail domain of COX2 contains the apoCuA site, the proper orientation of the ternary COX20–COX2-COX18 complex is crucial for recruiting protein adaptors SCO1, SCO2, and COA6, which mediate the insertion of two copper atom [53,54] (Fig. 1). In line, yeast COX18-KO shows no interaction between COX2 and COA6 and, consequently, a lack of CIV assemblies. Therefore, the decreased COX activity in mitochondria from the patient's fibroblasts could be due to a hindered interaction between COX20, COX2 and truncated COX18 complex that, in turn, affects the incorporation of copper in COX2 [55,56]. Previously, it has been reported that patient cell lines, which exhibit COX deficiency caused by pathogenic variants in the genes encoding SCO1, SCO2, and COA6, either partially or fully restore the enzymatic activity of cells upon copper treatment [57]. Future experiments are necessary to be explored the role of the truncated COX18 in the metalation of the binuclear Cu_A center.

The newly-described pathogenic variant COX18Δ112-240 causes a similar phenotype than that of the homozygous variant recently described at position 223 in COX18 (p.Asp223His) [26]. The pathogenic role of this variant could also be explained by the protonation of His223 could change its pK_a, which would affect the insertion of the third transmembrane domain of COX18 into the IMM (Fig. S5). This is turn could affect the molecular recognition with COX2, similar to our proposal for the COX2:COX18Δ112-240 complex. Thus, the results of our docking analysis of the only two pathogenic variants described so far for the *COX18* support a similar explanation for the altered function of this CIV assembly factor.

Despite the low probability of finding *COX18* pathogenic variants as a cause of reduced CIV activity [25], we would recommend carefully searching for variants in this gene in any infantile or neonatal case with signs of severe neurodegeneration, associated or not to cardiomyopathy, regardless of absence of ragged-red fibers in muscle biopsy, and even in cases of repeated spontaneous abortions, to reduce the incidence of new cases of this severe and devastating condition.

CRediT authorship contribution statement

Fabiola Mavillard: Writing – original draft, Supervision, Software, Methodology, Investigation, Formal analysis, Data curation, Conceptualization. **Alejandra Guerra-Castellano:** Writing – review & editing, Writing – original draft, Methodology, Investigation, Formal analysis, Data curation, Conceptualization. **David Guerrero-Gómez:** Methodology, Investigation, Formal analysis. **Eloy Rivas:** Methodology, Investigation. **Gloria Cantero:** Methodology, Investigation, Funding acquisition. **Emilia Servian-Morilla:** Methodology, Investigation, Funding acquisition. **Chiara Folland:** Formal analysis, Data curation. **Gianina Ravenscroft:** Formal analysis, Data curation. **Miguel A. Martín:** Methodology, Investigation. **Antonio Miranda-Vizuete:** Methodology, Investigation, Formal analysis. **Macarena Cabrera-Serrano:** Data curation, Conceptualization. **Irene Diaz-Moreno:** Writing – review & editing, Writing – original draft, Supervision, Resources, Project administration, Funding acquisition, Conceptualization. **Carmen Paradas:** Writing – review & editing, Writing – original draft, Supervision, Resources, Project administration, Funding acquisition, Conceptualization.

Declaration of competing interest

The authors declare that they have no known competing financial interests or personal relationships that could have appeared to influence the work reported in this paper.

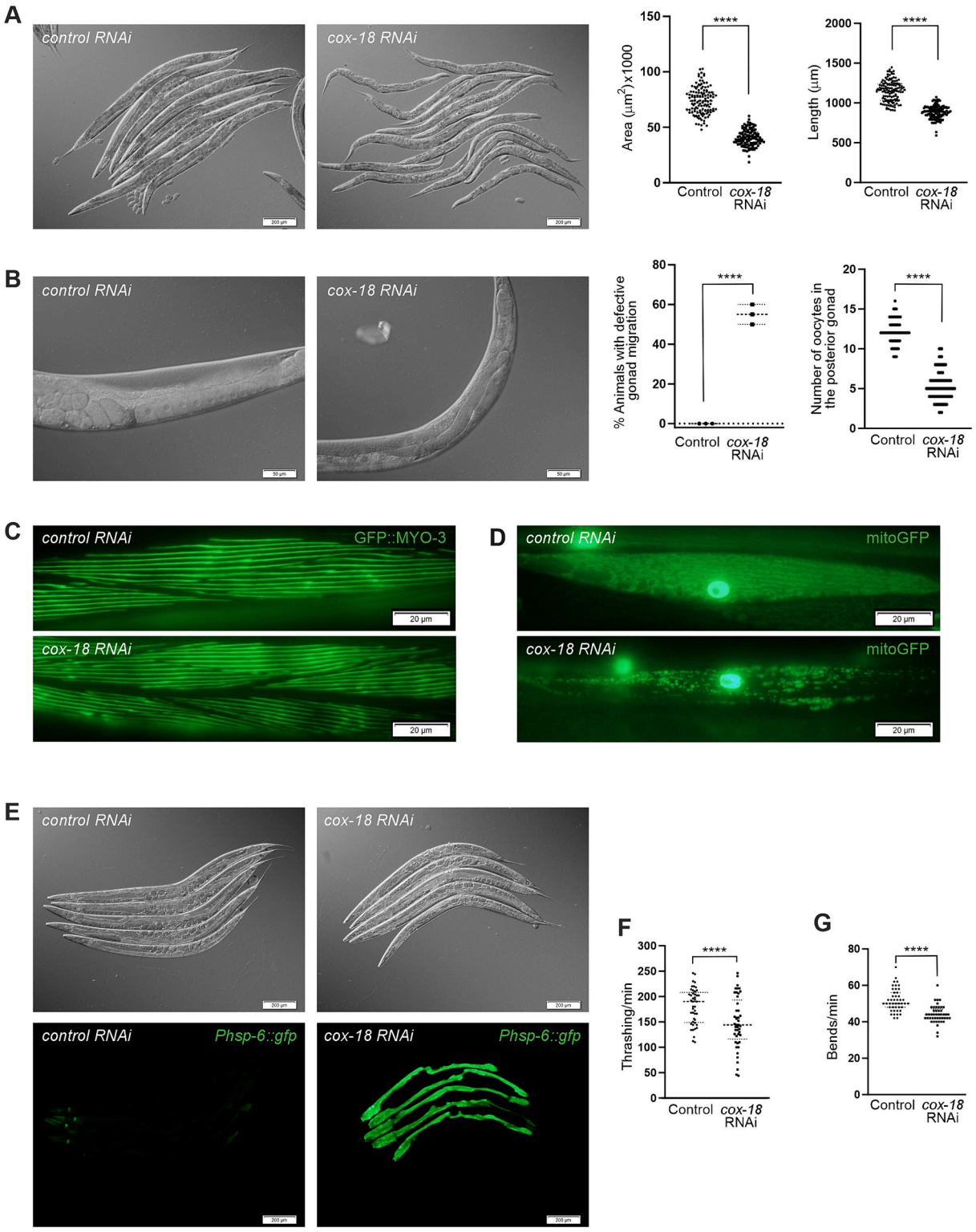

Fig. 7. Phenotypic characterization of *cox-18* downregulation in *C. elegans*. Feeding RNAi downregulation of *cox-18* in a *rrf-3(pk1426)* mutant background. A. Reduction of *cox-18* expression results in animals with a sick and less turgid appearance, with a significant reduction in body length and body area compared to control animals. B. Morphologically, animals show aberrant gonadal migration and reduced oocyte production. C–D. Downregulation of *cox-18* expression caused a strong fragmentation of the mitochondrial network of muscle cells with normal sarcomeres. E. Reduction of *cox-18* expression causes a robust induction of mitochondrial unfolded protein response (UPRmt). F–G. *cox-18* downregulated animals exhibit diminished muscular function measured as motility of worms in both liquid and solid medium.

Data availability

Data will be made available on request.

Acknowledgements

The authors acknowledge the patient and his family, as well as the patient association ASENSE for all the support to this work. We also acknowledge the facilities and scientific and technical assistance of CITIUS (University of Seville) and the Biomolecular Mass Spectrometry Service of the Pablo de Olavide University. This work was supported in part by the Instituto de Salud Carlos III (FIS PI19-01497 to C. Paradas), Consejería de Salud y Familia, Junta de Andalucía and Programa Operativo Fondo Social Europeo de Andalucía 2014–2020 (RH0046-2020 to G.C) and Consejería de Salud y Consumo, Junta de Andalucía and Programa Nicolas Monarde (C1-0003-2022 to E.S-M). We also acknowledge the FP7 WeNMR (project# 261572), H2020 West-Life (project# 675858), the EOSC-hub (project# 777536) and the EGI-ACE (project# 101017567) European e-Infrastructure projects for the use of their web portals, which make use of the EGI infrastructure with the dedicated support of CESNET-MCC, INFN-LNL-2, NCG-INGRID-PT, TW-NCHC, CESGA, IFCA-LCG2, UA-BITP, TR-FC1-ULAKBIM, CSTCLOUD-EGI, IN2P3-CPPM, CIRMMP, SURFsara and NIKHEF, and the additional support of the national GRID Initiatives of Belgium, France, Italy, Germany, the Netherlands, Poland, Portugal, Spain, UK, Taiwan and the US Open Science Grid. This work was supported by the Spanish Government (PGC2018-096049-B-I00, FEDER/Ministerio de Ciencia e Innovación — Agencia Estatal de Investigación Grant PID2021-126663NB-I00 funded by MCIN/AEI/10.13039/501100011033 and by ERDF A way of making Europe), European Regional Development Fund (FEDER), Andalusian Government (BIO-198, US/JUNTA/FEDER) and the Ramón Areces Foundation (2021–2024 to I.D.-M.). Some of the authors are part of the European Research Network in Neuromuscular Diseases (EURO-NMD).

Appendix A. Supplementary data

Supplementary data to this article can be found online at https://doi.org/10.1016/j.bbadis.2024.167330.

References

[1] L.D. Osellame, T.S. Blacker, M.R. Duchen, Cellular and molecular mechanisms of mitochondrial function, Best Pract. Res. Clin. Endocrinol. Metab. 26 (6) (2012) 711–723, https://doi.org/10.1016/J.BEEM.2012.05.003.

[2] H. Schägger, Respiratory chain supercomplexes of mitochondria and bacteria, Biochim. Biophys. Acta Bioenerg. 1555 (1–3) (2002) 154–159, https://doi.org/10.1016/S0005-2728(02)00271-2.

[3] A. Guerra-Castellano, A. Díaz-Quintana, B. Moreno-Beltrán, et al., Mimicking tyrosine phosphorylation in human cytochrome c by the evolved tRNA synthetase technique, Chemistry 21 (42) (2015) 15004–15012, https://doi.org/10.1002/CHEM.201502019.

[4] T.M. Sirey, C.P. Ponting, Insights into the post-transcriptional regulation of the mitochondrial electron transport chain, Biochem. Soc. Trans. 44 (5) (2016) 1491–1498, https://doi.org/10.1042/BST20160100.

[5] S. Cogliati, I. Lorenzi, G. Rigoni, F. Caicci, M.E. Soriano, Regulation of mitochondrial electron transport chain assembly, J. Mol. Biol. 430 (24) (2018) 4849–4873, https://doi.org/10.1016/J.JMB.2018.09.016.

[6] A. Díaz-Quintana, G. Pérez-Mejías, A. Guerra-Castellano, M.A. De La Rosa, I. Díaz-Moreno, Wheel and deal in the mitochondrial inner membranes: the tale of cytochrome c and cardiolipin, Oxidative Med. Cell. Longev. 2020 (2020), https://doi.org/10.1155/2020/6813405.

[7] I.J. Holt, A.E. Harding, J.A. Morgan-Hughes, Deletions of muscle mitochondrial DNA in patients with mitochondrial myopathies, Nature 331 (6158) (1988) 717–719, https://doi.org/10.1038/331717A0.

[8] R.M. Chalmers, A.H.V. Schapira, Clinical, biochemical and molecular genetic features of Leber's hereditary optic neuropathy, Biochim. Biophys. Acta 1410 (2) (1999) 147–158, https://doi.org/10.1016/S0005-2728(98)00163-7.

[9] L.A. Gómez, J.S. Monette, J.D. Chavez, C.S. Maier, T.M. Hagen, Supercomplexes of the mitochondrial electron transport chain decline in the aging rat heart, Arch. Biochem. Biophys. 490 (1) (2009) 30–35, https://doi.org/10.1016/J.ABB.2009.08.002.

[10] M.D. Brand, A.L. Orr, I. Perevoshchikova V, C.L. Quinlan, The role of mitochondrial function and cellular bioenergetics in ageing and disease, Br. J. Dermatol. 169 (Suppl 2(02)) (2013) 1–8, https://doi.org/10.1111/BJD.12208.

[11] S. Arnold, B. Kadenbach, Cell respiration is controlled by ATP, an allosteric inhibitor of cytochrome-c oxidase, Eur. J. Biochem. 249 (1) (1997) 350–354, https://doi.org/10.1111/J.1432-1033.1997.T01-1-00350.X.

[12] M. Bourens, A. Barrientos, Human mitochondrial cytochrome c oxidase assembly factor COX18 acts transiently as a membrane insertase within the subunit 2 maturation module, J. Biol. Chem. 292 (19) (2017) 7774–7783, https://doi.org/10.1074/JBC.M117.778514.

[13] M. Brischigliaro, M. Zeviani, Cytochrome c oxidase deficiency, Biochim. Biophys. Acta Bioenerg. 1862 (1) (2021), https://doi.org/10.1016/J.BBABIO.2020.148335.

[14] N. Brix, J.M. Jensen, I.S. Pedersen, et al., Mitochondrial disease caused by a novel homozygous mutation (Gly106del) in the SCO1 gene, Neonatology 116 (3) (2019) 290–294, https://doi.org/10.1159/000499488.

[15] C. Cerqua, V. Morbidoni, M.A. Desbats, et al., COX16 is required for assembly of cytochrome c oxidase in human cells and is involved in copper delivery to COX2, Biochim. Biophys. Acta Bioenerg. 1859 (4) (2018) 244–252, https://doi.org/10.1016/J.BBABIO.2018.01.004.

[16] S. Chakravorty, R. Logan, M.J. Elson, R.R. Luke, S. Verma, Expanding the genotype-phenotype correlation of childhood sensory polyneuropathy of genetic origin, Sci. Rep. 10 (1) (2020), https://doi.org/10.1038/S41598-020-73219-5.

[17] H.L. Dong, Y. Ma, H. Yu, et al., Bi-allelic loss of function variants in COX20 gene cause autosomal recessive sensory neuronopathy, Brain 144 (8) (2021) 2457–2470, https://doi.org/10.1093/BRAIN/AWAB135.

[18] S. Doss, K. Lohmann, P. Seibler, et al., Recessive dystonia-ataxia syndrome in a Turkish family caused by a COX20 (FAM36A) mutation, J. Neurol. 261 (1) (2014) 207–212, https://doi.org/10.1007/S00415-013-7177-7.

[19] A. Fire, S. Xu, M.K. Montgomery, S.A. Kostas, S.E. Driver, C.C. Mello, Potent and specific genetic interference by double-stranded RNA in *Caenorhabditis elegans*, Nature 391 (6669) (1998) 806–811, https://doi.org/10.1038/35888.

[20] D. Fornuskova, L. Stiburek, L. Wenchich, K. Vinsova, H. Hansikova, J. Zeman, Novel insights into the assembly and function of human nuclear-encoded cytochrome c oxidase subunits 4, 5a, 6a, 7a and 7b, Biochem. J. 428 (3) (2010) 363–374, https://doi.org/10.1042/BJ20091714.

[21] A. Signes, E. Fernandez-Vizarra, Assembly of mammalian oxidative phosphorylation complexes I–V and supercomplexes, Essays Biochem. 62 (3) (2018) 255–270, https://doi.org/10.1042/EBC20170098.

[22] A. Timón-Gómez, E. Nývltová, L.A. Abriata, A.J. Vila, J. Hosler, A. Barrientos, Mitochondrial cyto- chrome c oxidase biogenesis: recent developments, Semin. Cell Dev. Biol. 76 (2018) 163–178, https://doi.org/10.1016/J.SEMCDB.2017.08.055.

[23] K. Hell, A. Tzagoloff, W. Neupert, R.A. Stuart, Identification of Cox20p, a novel protein involved in the maturation and assembly of cytochrome oxidase subunit 2, J. Biol. Chem. 275 (7) (2000) 4571–4578, https://doi.org/10.1074/JBC.275.7.4571.

[24] M. Bourens, A. Boulet, S.C. Leary, A. Barrientos, Human COX20 cooperates with SCO1 and SCO2 to mature COX2 and promote the assembly of cytochrome c oxidase, Hum. Mol. Genet. 23 (11) (2014) 2901–2913, https://doi.org/10.1093/HMG/DDU003.

[25] S. Sacconi, L. Salviati, E. Trevisson, Mutation analysis of COX18 in 29 patients with isolated cytochrome c oxidase deficiency, J. Hum. Genet. 54 (7) (2009) 419–421, https://doi.org/10.1038/JHG.2009.36.

[26] D. Ronchi, M. Garbellini, F. Magri, et al., A biallelic variant in COX18 cause isolated complex IV deficiency associated with neonatal encephalo-cardio-myopathy and axonal sensory neuropathy, Eur. J. Hum. Genet. 31 (12) (2023) 1414–1420, https://doi.org/10.1038/S41431-023-01433-6.

[27] A.J. Valente, L.A. Maddalena, E.L. Robb, F. Moradi, J.A. Stuart, A simple ImageJ macro tool for analyzing mitochondrial network morphology in mammalian cell culture, Acta Histochem. 119 (3) (2017) 315–326, https://doi.org/10.1016/J.ACTHIS.2017.03.001.

[28] S. Yoshida, S. Tsutsumi, G. Muhlebach, et al., Molecular chaperone TRAP1 regulates a metabolic switch between mitochondrial respiration and aerobic glycolysis, Proc. Natl. Acad. Sci. USA 110 (17) (2013), https://doi.org/10.1073/pnas.1220659110.

[29] C. Frezza, S. Cipolat, L. Scorrano, Organelle isolation: functional mitochondria from mouse liver, muscle and cultured filroblasts, Nat. Protoc. 2 (2) (2007) 287–295, https://doi.org/10.1038/nprot.2006.478.

[30] M.L. Huynh, P. Russell, B. Walsh, Tryptic digestion of in-gel proteins for mass spectrometry analysis, Methods Mol. Biol. 519 (2009) 507–513, https://doi.org/10.1007/978-1-59745-281-6_34.

[31] A. Guerra-Castellano, A. Díaz-Quintana, G. Pérez-Mejías, et al., Oxidative stress is tightly regulated by cytochrome c phosphorylation and respirasome factors in mitochondria, Proc. Natl. Acad. Sci. USA 115 (31) (2018) 7955–7960, https://doi.org/10.1073/PNAS.1806833115.

[32] T. Stiernagle, Maintenance of *C. elegans*, WormBook, 2006, pp. 1–11, https://doi.org/10.1895/wormbook.1.101.1. Published online.

[33] M. Peña-Chilet, G. Roldán, J. Perez-Florido, et al., CSVS, a crowdsourcing database of the Spanish population genetic variability, Nucleic Acids Res. 49 (D1) (2021) D1130–D1137, https://doi.org/10.1093/NAR/GKAA794.

[34] I.A. Adzhubei, S. Schmidt, L. Peshkin, et al., A method and server for predicting damaging missense mutations, Nat. Methods 7 (4) (2010) 248–249, https://doi.org/10.1038/NMETH0410-248.

[35] Y. Choi, G.E. Sims, S. Murphy, J.R. Miller, A.P. Chan, Predicting the functional effect of amino acid substitutions and indels, PLoS One 7 (10) (2012), https://doi.org/10.1371/JOURNAL.PONE.0046688.

[36] P.C. Ng, S. Henikoff, SIFT: predicting amino acid changes that affect protein function, Nucleic Acids Res. 31 (13) (2003) 3812–3814, https://doi.org/10.1093/NAR/GKG509.
[37] J.M. Schwarz, D.N. Cooper, M. Schuelke, D. Seelow, MutationTaster2: mutation prediction for the deep-sequencing age, Nat. Methods 11 (4) (2014) 361–362, https://doi.org/10.1038/NMETH.2890.
[38] X. Jian, E. Boerwinkle, X. Liu, In silico prediction of splice-altering single nucleotide variants in the human genome, Nucleic Acids Res. 42 (22) (2014) 13534–13544, https://doi.org/10.1093/NAR/GKU1206.
[39] H.A. Shihab, M.F. Rogers, J. Gough, et al., An integrative approach to predicting the functional effects of non-coding and coding sequence variation, Bioinformatics 31 (10) (2015) 1536–1543, https://doi.org/10.1093/BIOINFORMATICS/BTV009.
[40] A. Van Hoof, P.A. Frischmeyer, H.C. Dietz, R. Parker, Exosome-mediated recognition and degradation of mRNAs lacking a termination codon, Science 295 (5563) (2002) 2262–2264, https://doi.org/10.1126/SCIENCE.1067272.
[41] G.C.P. Van Zundert, J.P.G.L.M. Rodrigues, M. Trellet, et al., The HADDOCK2.2 web server: user-friendly integrative modeling of biomolecular complexes, J. Mol. Biol. 428 (4) (2016) 720–725, https://doi.org/10.1016/J.JMB.2015.09.014.
[42] P.L. Kastritis, A.M.J.J. Bonvin, On the binding affinity of macromolecular interactions: daring to ask why proteins interact, J. R. Soc. Interface 10 (79) (2012), https://doi.org/10.1098/RSIF.2012.0835.
[43] F. Simmer, M. Tijsterman, S. Parrish, et al., Loss of the putative RNA-directed RNA polymerase RRF-3 makes *C. elegans* hypersensitive to RNAi, Curr Biol. 12 (15) (2002) 1317–1319, https://doi.org/10.1016/s0960-9822(02)01041-2.
[44] F. Simmer, C. Moorman, A.M. Van Der Linden, et al., Genome-wide RNAi of *C. elegans* using the hypersensitive rrf-3 strain reveals novel gene functions, PLoS Biol. 1 (1) (2003) e12, https://doi.org/10.1371/JOURNAL.PBIO.0000012.
[45] S. Gandre, A.M. van der Bliek, Mitochondrial division in *Caenorhabditis elegans*, Methods Mol. Biol. 372 (2007) 485–501, https://doi.org/10.1007/978-1-59745-365-3_34.
[46] T. Yoneda, C. Benedetti, F. Urano, S.G. Clark, H.P. Harding, D. Ron, Compartment-specific perturbation of protein handling activates genes encoding mitochondrial chaperones, J. Cell Sci. 117 (Pt 18) (2004) 4055–4066, https://doi.org/10.1242/JCS.01275.
[47] M.A. Tarnopolsky, J.M. Bourgeois, M.H. Fu, et al., Novel SCO2 mutation (G1521A) presenting as a spinal muscular atrophy type I phenotype, Am. J. Med. Genet. A 125A (3) (2004) 310–314, https://doi.org/10.1002/ajmg.a.20466.
[48] A.P. Rebelo, D. Saade, C.V. Pereira, et al., SCO2 mutations cause early-onset axonal Charcot-Marie-tooth disease associated with cellular copper deficiency, Brain 141 (3) (2018) 662–672, https://doi.org/10.1093/brain/awx369.
[49] M.G. Otero, E. Tiongson, F. Diaz, et al., Novel pathogenic COX20 variants causing dysarthria, ataxia, and sensory neuropathy, Ann. Clin. Transl. Neurol. 6 (1) (2019) 154–160, https://doi.org/10.1002/acn3.661.
[50] S.C. Leary, H. Antonicka, F. Sasarman, et al., Novel mutations in SCO1 as a cause of fatal infantile encephalopathy and lactic acidosis, Hum. Mutat. 34 (10) (2013) 1366–1370, https://doi.org/10.1002/HUMU.22385.
[51] I. Valnot, S. Osmond, N. Gigarel, et al., Mutations of the SCO1 gene in mitochondrial cytochrome c oxidase deficiency with neonatal-onset hepatic failure and encephalopathy, Am. J. Hum. Genet. 67 (5) (2000) 1104–1109, https://doi.org/10.1016/S0002-9297(07)62940-1.
[52] J. Gurgel-Giannetti, G. Oliveira, G.B. Filho, P. Martins, M. Vainzof, M. Hirano, Mitochondrial cardio-encephalomyopathy due to a novel SCO2 mutation in a Brazilian patient: case report and literature review, JAMA Neurol. 70 (2) (2013) 258–261, https://doi.org/10.1001/JAMANEUROL.2013.595.
[53] K.A. Jett, S.C. Leary, Building the CuA site of cytochrome c oxidase: a complicated, redox-dependent process driven by a surprisingly large complement of accessory proteins, J. Biol. Chem. 293 (13) (2018) 4644–4652, https://doi.org/10.1074/JBC.R117.816132.
[54] E. Nývltová, J.V. Dietz, J. Seravalli, O. Khalimonchuk, A. Barrientos, Coordination of metal center biogenesis in human cytochrome c oxidase, Nat. Commun. 13 (1) (2022), https://doi.org/10.1038/S41467-022-31413-1.
[55] L.E. Elliott, S.A. Saracco, T.D. Fox, Multiple roles of the Cox20 chaperone in assembly of *Saccharomyces cerevisiae* cytochrome c oxidase, Genetics 190 (2) (2012) 559–567, https://doi.org/10.1534/GENETICS.111.135665.
[56] D. Pacheu-Grau, B. Bareth, J. Dudek, et al., Cooperation between COA6 and SCO2 in COX2 maturation during cytochrome c oxidase assembly links two mitochondrial cardiomyopathies, Cell Metab. 21 (6) (2015) 823–833, https://doi.org/10.1016/J.CMET.2015.04.012.
[57] A. Casarin, G. Giorgi, V. Pertegato, et al., Copper and bezafibrate cooperate to rescue cytochrome c oxidase deficiency in cells of patients with SCO2 mutations, Orphanet J. Rare Dis. 7 (1) (2012), https://doi.org/10.1186/1750-1172-7-21.